Exact muffin tin orbital based first-principles method for electronic-structure and electron-transport simulation of device materials

Qingyun Zhang, Jiawei Yan, Yu Zhang, and Youqi Ke*
School of Physical Science and Technology, ShanghaiTech University, Shanghai 201210, China

(Received 20 May 2019; revised manuscript received 27 July 2019; published 16 August 2019)

The exact muffin tin orbital (EMTO) method features high efficiency and accuracy for first-principles simulations with density functional theory. In this paper we report our implementation of the EMTO method for electronic-structure and quantum transport simulation of device materials. We consider a device-material structure with a central device region in contact with different semi-infinite electrodes. Based on the Green's function method, the infinite device, nonperiodic in transport direction, is transformed into a calculable finite material system by treating the semi-infinite electrodes with electrode self-energies, and the Green's function of the device region is calculated with an efficient recursive technique. In the present implementation we adopt the spherical cell approximation to treat the electrostatics, and we solve the electrostatic potential of the finite device region by enforcing the boundary conditions to the known potential of electrode materials. The coherent potential approximation is incorporated for treating the atomic disorders inevitable in realistic materials, and the effects of multiple disorder scattering on electron transport are accounted for by vertex correction for simulating disordered electronic devices. To demonstrate the capability of the present implementation, we calculate the monolayer two-dimensional material MoS_2 and black phosphorus, and study the spin-dependent tunneling in the Fe/MgO/Fe magnetic tunneling junction. We find the EMTO electronic structures of the calculated systems agree well with the results of the projector augmented wave method. The EMTO transport simulation produces the important spin-filtering effect of the Fe/MgO/Fe junction and the important influence of the interfacial disorders on the spin-dependent tunneling, agreeing well with previous theoretical and experimental studies. The implementation of the EMTO based device simulator provides an effective simulation tool for simulating both ordered and disordered device materials, extending the capability for theoretical design of electronic devices from first principles.

DOI: 10.1103/PhysRevB.100.075134

I. INTRODUCTION

As continuing the miniaturization of device size, the atomic discretization and quantum nature of the electron play important roles in device functionality, especially at nanoscale [1]. Therefore, the development of first-principles device-materials simulation is of great importance for understanding the effects of different materials, interfaces, and disordered defects/impurities on device performance, and realizing theoretical material design for device applications [2–4]. Presently, density functional theory (DFT) based on the Kohn-Sham (KS) ansatz [5,6] has been built as the workhorse for first-principles material study in chemistry, condensed matter physics, and material science and engineering. Many advanced methods, including linearized augmented plane wave method [7,8], projector augmented wave method (PAW) [9], linear combination of atomic orbital method [10], real-space finite-difference method [11], etc., have been developed to solve the KS equation with important successes. However, the standard implementations of KSDFT are based on a periodic or closed boundary condition, for example the widely used software packages VASP [12], WIEN2K [13], etc., and thus face important difficulties for simulating disorders, polar surfaces [14], interfaces, and material systems with open boundary conditions, presenting great challenges for the simulations of operating devices.

Nevertheless, the Green's function technique provides an important approach for treating complex systems with various mean-field theories [15–17] and a diagrammatic technique of many-body perturbation [18]. The implementation of KS-DFT in combination with the Green's function method provides a sophisticated framework for realizing the first-principles simulation of realistic materials and devices with complex physical conditions, significantly extending the capability of KSDFT beyond the standard implementations [19–29]. Among the different implementations of the first-principles Green's function method [19,20,22–29], the methods based on different generations of muffin tin (MT) orbital proposed by Andersen and his co-workers [30–37] are the representatives. Compared to other basis functions, the MTO since the second generation features important advantages: (i) all-electron calculation overcomes pseudopotential approximation for core electrons; (ii) the screened MTO is very localized in real space, making the Hamiltonian matrix sparse; (iii) MTO basis sets are minimal; and (iv) coherent potential approximation (CPA) for treating atomic disorders inevitable in realistic devices can be easily incorporated in Green's function formalism. With these important advantages, the second generation of MTO, namely TB-LMTO method,

*keyq@shanghaitech.edu.cn

has been widely used for the simulation of electronic structures, and electron/spin transport properties of multilayered structures with important successes [2–4,21,38]. However, the implementation of the TB-LMTO method possesses important limitations in applicability due to two major problems: The first is that the linearization of the basis function causes an important error at the energy distant from the linearization reference energy; the second error arises from the used atomic sphere approximation (ASA) which utilizes spherically symmetric potentials inside each space-filling atomic sphere and neglects the contribution of the interstitial region for simplicity.

Recently, the third generation of MTO, called exact muffin tin orbital (EMTO) [34,37], has been proposed with important major improvements over the TB-LMTO method, including: (i) the large overlapping potential spheres provide more accurate representation of the potential of the material system; (ii) the interstitial region is treated on the same footing as the atomic region; and (iii) energy linearization is not required within the Green's function formalism. Based on these improvements and the advantages of MTO listed above, EMTO possesses an important potential for application in the electronic-structure and electron-transport simulation of realistic materials and devices. Presently, Vitos *et al.* [39–43] has successfully realized the EMTO based self-consistent electronic-structure calculation for bulk systems, and proved its high efficiency and accuracy for a wide range of applications [44–53]. Their results of the EMTO method showed very good agreement with other all-electron methods, such as full-potential linear augmented wave method. However, presently, the implementation of EMTO is only limited to the bulk periodic structures. The first-principles EMTO simulation of materials on the device level requires significant extensions on the implementation of the EMTO method.

In this work we report our implementation of the EMTO based KSDFT to realize the electronic-structure and quantum transport simulation of electronic devices containing atomic disorders from first principles. We consider a device-materials structure containing a central device region in contact with different semi-infinite electrodes. Within the Green's function method, the influences of the semi-infinite electrodes on the central device interested are accounted for by the contact self-energies, making the infinite device system into a calculable finite system. The electronic structures of the electrode materials are calculated by the EMTO bulk solver and kept fixed in the self-consistent calculation of the central region. By dividing the system into principle layers, we apply the recursive Green's function technique to efficiently calculate the device region. To effectively treat atomic disorders, coherent potential approximation is incorporated to calculate the disorder averaged electronic structure. In the transport calculation, the averaged transmission function is calculated by accounting for the effects of multiple disorder scattering with vertex corrections within the CPA. As a demonstration of our implementation of EMTO for device-materials simulation, we calculate the electronic structure of MoS_2, black phosphorus, and the spin-dependent quantum transport properties of Fe/MgO/Fe magnetic tunneling junctions (MTJs). We compare our result with the calculations of PAW method by using VASP [12].

The rest of the paper is organized as follows. Section II presents the formalism of exact muffin tin orbital method. In Sec. III, the Green's function method is presented to calculate the multilayered two-probe device structure in contact with electrodes. In Sec. IV, coherent potential approximation is incorporated to treat systems with disordered defects/impurities. Section V introduces the calculation of the transmission coefficient with vertex corrections to account for the multiple disorder scattering, to realize the quantum transport simulation of disordered nanoelectronics. Section VI discusses the self-consistent implementation of the whole algorithm, including the calculation of electron density and effective potential. In Sec. VII we discuss the applications to bulk MoS_2 and black phosphorus, and two-probe Fe/MgO/Fe MTJs. Finally, we conclude our work in Sec. VIII and provide more information in the Appendix.

II. EXACT MUFFIN TIN ORBITAL METHOD

A. Exact muffin tin orbital

In the muffin tin potential approximation, the effective full potential is approximated as

$$V(\boldsymbol{r}) \approx V_{mt}(\boldsymbol{r}) \equiv V_{mtz} + \sum_R [V_R(r_R) - V_{mtz}], \tag{1}$$

where $V_R(r_R)$ is the spherical potential well centered on each lattice site R and V_{mtz} is a constant potential. (Here and in the following, we use the notation $\boldsymbol{r}_R = \boldsymbol{r} - \boldsymbol{R}$, and $r_R = \mid \boldsymbol{r}_R \mid$.) Different from the conventional nonoverlapping muffin tin spheres, the EMTO method utilizes the large overlapping potential spheres which gives more accurate description of the potential compared to the conventional approximation, especially for the interstitial region. As a result, the EMTO method treats the interstitial and atomic regions on the same footing, and thus can provide high accuracy for describing disordered systems, interfaces/surfaces, and material structures with low symmetry, beyond the second generation TB-LMTO method.

The energy dependent EMTO is composed of three parts as follows:

$$\Phi^a_{RL}(\epsilon, \mathbf{r}_R) = \phi^a_{RL} - \varphi^a_{RL} + \psi^a_{RL}, \tag{2}$$

including the partial wave ϕ^a_{RL}, free electron solution φ^a_{RL}, and screened spherical wave (SSW) ψ^a_{RL}. Here the superscript a denotes the screening representation (here we only provide a brief introduction of EMTO for completeness, for more details, please refer to the literatures [34–37,39,40,42]). The partial wave ϕ^a_{RL} defined inside each overlapping potential sphere (s_R) is solved from the local Schrödinger equation [54] with the potential $V_R(r_R)$. The SSW ϕ^a_{RL}, served as the envelope function, satisfies the interstitial Schrödinger equation, namely $[\nabla^2 + \kappa^2]\psi^a_{RL}(\kappa^2, \mathbf{r}_R) = 0$, where $\kappa^2 = \epsilon - V_{mtz}$ is the kinetic energy. It is known that the SSW can be generally expanded around other sites R' in the form

$$\psi^a_{RL}(\kappa^2, \mathbf{r}_R) = n^a_{RL}(\kappa^2, \mathbf{r}_R)\delta_{RR'} + \sum_{R'L'} j^a_{R'L'}(\kappa^2, \mathbf{r}_{R'}) S^a_{R'L',RL}(\kappa^2), \tag{3}$$

where n^a_{RL} and j^a_{RL} are the respective head and tail functions and S^a is the corresponding screened slope matrix. Different

from the second generation MTO [37], SSW is obtained by adopting the general screening strategy of the Methfessel formulation [55], namely introducing a set of nonoverlapping screening spheres with radius a_{Rl}, and then imposing boundary conditions so that it equals pure spherical harmonics on its own a sphere and vanishes on and inside the other a spheres ($n^a_{Rl}|_a = 1.0$, $j^a_{Rl}|_a = 0.0$) [34–37,39,40,42]. SSWs are continuous but not differentiable, presenting kinks on the screening spheres.

The free electron solution φ^a_{RL} is defined in the region between the screening and potential spheres as [34–37,39,40,42]

$$\varphi^a_{Rl}(\epsilon, r_R) = n^a_{Rl}(\kappa^2, r_R) + j^a_{Rl}(\kappa^2, r_R) D^a_{Rl}(\epsilon), \tag{4}$$

where $D^a_{Rl}(\epsilon) = D^a_{Rl}\{\varphi^a_{Rl}\}$ is the logarithmic derivative of the free-electron solution at a_{Rl}. By introducing φ^a_{RL}, EMTO in Eq. (2) satisfies the proper boundary conditions that the function is continuous at both a_R and s_R, and differentiable at s_R.

B. The overlap and Hamiltonian matrices and Green's function

Within the EMTO, the overlap matrix $\langle\Phi^a|\Phi^a\rangle$ can be approximated as [34–37]

$$\begin{aligned}\langle\Phi^a|\Phi^a\rangle &= \langle\phi^a - \varphi^a + \psi^a|\phi^a - \varphi^a + \psi^a\rangle \\ &\approx \langle\phi^a|\phi^a\rangle - \langle\varphi^a|\varphi^a\rangle + \langle\psi^a|\psi^a\rangle\end{aligned} \tag{5}$$

in which the contribution of the terms $\langle\phi^a - \varphi^a|\psi^a - \varphi^a\rangle$ and $\langle\psi^a - \varphi^a|\phi^a - \varphi^a\rangle$ are neglected since they are very small [$\sim o(s-a)^4$] [35]. By applying the Green's second identity [56], one can obtain $\langle\phi^a|\phi^a\rangle - \langle\varphi^a|\varphi^a\rangle = -a\dot{D}^a(\epsilon)$, where $\dot{D}(\epsilon, s) \equiv \frac{\partial D(\epsilon,s)}{\partial \epsilon}$ is site diagonal. Furthermore, one can also find $\langle\psi^a|\psi^a\rangle = a\dot{S}^a(\epsilon)$, in which $\dot{S}^a$ is the energy derivative of the slope matrix. As a result, we obtain the overlap matrix in EMTO:

$$\langle\Phi^a|\Phi^a\rangle = -a\dot{D}^a(\epsilon) + a\dot{S}^a(\epsilon) = \dot{K}^a(\epsilon). \tag{6}$$

Where $K = aS^a - aD^a$ is called the kink matrix.

Instead of finding the Hamiltonian matrix $\langle\Phi^a|H|\Phi^a\rangle$, we derive the matrix $\langle\Phi^a|H-\epsilon|\Phi^a\rangle$. Similar to the overlap matrix, we have

$$\begin{aligned}\langle\Phi^a|H-\epsilon|\Phi^a\rangle \approx{}& \langle\phi^a|H-\epsilon|\phi^a\rangle - \langle\varphi^a|H-\epsilon|\varphi^a\rangle \\ &+ \langle\psi^a|H-\epsilon|\psi^a\rangle.\end{aligned} \tag{7}$$

By referring to the literature [34–37], one can find the first two terms in Eq. (7) $\langle\phi^a|H-\epsilon|\phi^a\rangle - \langle\varphi^a|H-\epsilon|\varphi^a\rangle = aI + aD^a(\epsilon)$, and the third term is given as $\langle\psi^a|H-\epsilon|\psi^a\rangle = -aI - aS^a(\epsilon)$, where I is the identity matrix. As a result, we obtain

$$\langle\Phi^a|H-\epsilon|\Phi^a\rangle = aD^a(\epsilon) - aS^a(\epsilon) = -K^a(\epsilon). \tag{8}$$

It is clear that the K^a is as short ranged as the screened slop matrix S^a, providing the high efficiency for the computation with the EMTO method. After obtaining overlap and Hamiltonian matrices, the Green's function is then defined for a complex energy z by

$$g^a(z) = K^a(z)^{-1}, \tag{9}$$

and the corresponding normalized Green's function is given as

$$G(z) = g^a(z)\dot{K}^a(z). \tag{10}$$

With the above Green's functions, the physical properties of materials and devices can be efficiently calculated with the EMTO method.

III. GREEN'S FUNCTION FORMALISM FOR TWO-PROBE DEVICES

In this section we shall focus on calculating the Green's function in Eq. (9) for the two-probe electronic device system. The two-probe device consists of a central device region sandwiched by the left and right semi-infinite electrodes as shown in Fig. 1. The electron can transport through the central device region with scattering by interface and defects from one electrode to the other. The system features periodicity in x-y plane, but nonperiodicity in the infinite transport z direction (note, for a disordered system, configurational average restores the translation invariance). By using sufficiently long buffer layers of electrode materials in the central region, the electronic structure of electrodes could not be affected by the central region. As an important consequence, we can use the electronic potential self-consistently calculated by the EMTO bulk solver for the electrode materials in the device system. Therefore, we only need to determine the electronic structure in the central device region to obtain the physical properties of the whole device system, such as the electron-transport property. To obtain the Green's function of the central region, we rewrite Eq. (9) for a two-probe device (we omit ϵ in the following for simplicity),

$$\begin{pmatrix} K^a_{ll} & K^a_{lc} & 0 \\ K^a_{cl} & K^a_{cc} & K^a_{cr} \\ 0 & K^a_{rc} & K^a_{rr} \end{pmatrix} \begin{pmatrix} g^a_{ll} & g^a_{lc} & g^a_{lr} \\ g^a_{cl} & g^a_{cc} & g^a_{cr} \\ g^a_{rl} & g^a_{rc} & g^a_{rr} \end{pmatrix} = \begin{pmatrix} I_l & 0 & 0 \\ 0 & I_c & 0 \\ 0 & 0 & I_r \end{pmatrix}, \tag{11}$$

where K_{ll}, K_{cc}, and K_{rr} describe the left electrode, central device, and right electrode, respectively, and $K_{lc/cl}$ and $K_{rc/cr}$ represent the couplings of the central device region with the respective left and right electrodes. the left and right electrodes are separated too far to have couplings. Here we are only interested in the Green's function of the central region

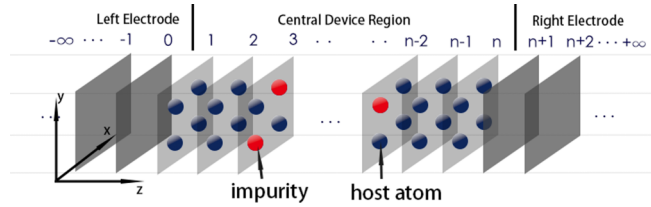

FIG. 1. Schematic illustration of two-probe device containing a central device region contacting to the left and right electrodes. The system is divided into different principle layers: $ip \leqslant 0$ for the left electrode, $1 \leqslant ip \leqslant np$ for the central device region, and $ip \geqslant np+1$ for the right electrode.

g^a_{cc}, for which one can find the following equations:

$$K^a_{ll}\mathrm{g}^a_{lc} + K^a_{lc}\mathrm{g}^a_{cc} = 0, \tag{12}$$

$$K^a_{cl}\mathrm{g}^a_{lc} + K^a_{cc}\mathrm{g}^a_{cc} + K^a_{cr}\mathrm{g}^a_{rc} = I_c, \tag{13}$$

$$K^a_{rc}\mathrm{g}^a_{cc} + K^a_{rr}\mathrm{g}^a_{rc} = 0. \tag{14}$$

Eliminating g^a_{lc} and g^a_{rc} in the above equations leads to

$$\mathrm{g}^a_{cc} = \left\{K^a_{cc} - \Sigma^a_l - \Sigma^a_r\right\}^{-1}, \tag{15}$$

$$\Sigma^a_l = K^a_{cl}\mathrm{g}^{a,0}_{ll}K^a_{lc}, \tag{16}$$

$$\Sigma^a_r = K^a_{cr}\mathrm{g}^{a,0}_{rr}K^a_{rc}, \tag{17}$$

$$\mathrm{g}^{a,0}_{ll} = K^{a,-1}_{ll}, \tag{18}$$

$$\mathrm{g}^{a,0}_{rr} = K^{a,-1}_{rr}. \tag{19}$$

Where the quantity $\Sigma^a_{l/r}$ refers to the self-energies describing the effects of the semi-infinite left/right electrode to the central region, and $\mathrm{g}^{a,0}_{ll/rr}$ is the Green's functions of the completely separated electrodes. With Eq. (15) we transform the infinite nonperiodic two-probe device to a calculable finite system with the self-energies describing the effects of electrodes.

To make the calculation of g^a_{cc} in Eq. (15) and related quantities practical, we divide the two-probe system into a set of principal layers (PLs) along the z axis [57]. As shown in Fig. 1, the central device region contains PLs with the indices $ip = 1, 2, \ldots, n-1, n$, while left and right electrodes contain PLs $ip = 0, -1, \ldots, -\infty$ and $ip = n+1, n+2, \ldots, +\infty$, respectively. The size of each principle layer is chosen in such a way that only the nearest-neighbor PLs are coupled, namely the element of kink matrix $K_{ip,ip+m} = 0$ for any $m \geqslant 2$. As a result, the kink matrix becomes tridiagonal, allowing us to apply recursive technique to calculate g^a_{cc} in Eq. (15).

With the tridiagonal feature of K matrix in multilayer structures, $\Sigma^a_{l/r}$ in Eqs. (16) and (17) have the explicit form [58]

$$\Sigma^a_l = K^a_{cl}\mathrm{g}^{a,0}_{ll}K^a_{lc} = \begin{pmatrix} \Sigma^a_{l,11} & 0 & \cdots \\ 0 & 0 & \cdots \\ \vdots & \vdots & \ddots \end{pmatrix}, \tag{20}$$

$$\Sigma^a_r = K^a_{cr}\mathrm{g}^{a,0}_{rr}K^a_{rc} = \begin{pmatrix} \ddots & \vdots & \vdots \\ \cdots & 0 & 0 \\ \cdots & 0 & \Sigma^a_{r,NN} \end{pmatrix}. \tag{21}$$

Only (11) and (NN) on-layer blocks are nonzero for the self-energies Σ^a_l and Σ^a_r, respectively, which can be obtained from

$$\Sigma^a_{l,11} = K^a_{1,0}\mathrm{g}^{a,0}_{ll,00}K^a_{0,1}, \tag{22}$$

$$\Sigma^a_{r,NN} = K^a_{N,N+1}\mathrm{g}^{a,0}_{rr,N+1N+1}K^a_{N+1,N}, \tag{23}$$

in which $\mathrm{g}^{a,0}_{ll,00}$ and $\mathrm{g}^{a,0}_{rr,N+1N+1}$ are the surface Green's functions of the left and right electrodes, respectively [58]. We implement an efficient method called the renormalization-decimation technique to iteratively solve the surface Green's function to obtain the blocks $\Sigma^a_{l,11}$ and $\Sigma^a_{r,NN}$.

After obtaining the electrode self-energies Σ^a_l and Σ^a_r, the Green's function of central device region, namely g_{cc} in Eq. (15), can be calculated by inverting the tridiagonal matrix as follows:

$$g^a_{cc} = \begin{pmatrix} K^a_{1,1} - \Sigma^a_{l,11} & K^a_{1,2} & 0 & 0 & 0 & \\ K^a_{2,1} & K^a_{2,2} & K^a_{2,3} & 0 & 0 & \\ \vdots & \vdots & \ddots & \ddots & \ddots & \ddots \\ 0 & 0 & K^a_{n-1,n-2} & K^a_{n-1,n-1} & K^a_{n-1,n} & \\ 0 & 0 & 0 & K^a_{n,n-1} & K^a_{n,n} - \Sigma^a_{r,nn} & \end{pmatrix}^{-1}. \tag{24}$$

We will omit the subscript cc in the rest of the paper for simplicity (and will put it back if necessary). We adopt the recursive Green's function technique to efficiently calculate the layer-diagonal and off-diagonal blocks [59]. First, in the recursive technique, the layer-diagonal blocks can be given for any intermediate layers i in the form

$$g^a_{ii} = \left[K_{i,i} - \Sigma^l_i - \Sigma^r_i\right]^{-1} \quad (1 \leqslant i \leqslant n), \tag{25}$$

where Σ^l_i and Σ^r_i are also called self-energies describing the coupling of the ith layer with the respective left and right sides of the of system. The self-energies Σ^l_i and Σ^r_i both can be calculated independently in a recursive way by starting from the first and nth principle layers of the central device region. By starting from the first-principle layer (left side), namely by setting $\Sigma^l_1 = \Sigma_{l,11}$, we have

$$\Sigma^l_i = K^a_{i,i-1}\left[K^a_{i-1,i-1} - \Sigma^l_{i-1}\right]^{-1}K^a_{i-1,i}, \tag{26}$$

for i changing from 2 to n. Moreover, by setting $\Sigma^r_n = \Sigma_{r,nn}$, we calculate Σ^r_i with

$$\Sigma^r_i = K^a_{i,i+1}\left[K^a_{i+1,i+1} - \Sigma^r_{i+1}\right]^{-1}K^a_{i+1,i}, \tag{27}$$

for i changing from $n-1$ to 1.

Once the layer-diagonal block of the Green's function, i.e., g^a_{ii}, is found, with the recursive technique, the off-diagonal block of the Green's function can also be straightforwardly derived as follows:

$$g^a_{ij} = -\left[K^a_{i,i} - \Sigma^r_i\right]^{-1}K^a_{i,i-1}g^a_{i-1,j} \quad (i > j), \tag{28}$$

$$g^a_{ij} = -\left[K^a_{i,i} - \Sigma^l_i\right]^{-1}K^a_{i,i+1}g^a_{i+1,j} \quad (i < j). \tag{29}$$

The above results are general for calculating the inversion of the tridiagonal matrix, providing important convenience for simulating the layered structures.

Due to the periodicity in the x-y plane of the two-probe device, we can apply two-dimensional (2D) lattice Fourier transformation to the kink matrix so that

$$K^a_{p\mathbf{B},p'\mathbf{B}'}(\epsilon,\mathbf{k}_\parallel)=\sum_{T_\parallel} e^{i\mathbf{k}_\parallel T_\parallel} K^a_{p\mathbf{B},p'\mathbf{B}'+T_\parallel}(\epsilon) \tag{30}$$

in which $\mathbf{k}_\parallel$ is the wave vector in the 2D Brillouin zone, and $(p\mathbf{B}+T_\parallel)$ denotes the lattice vector. Here p is the index of the principle layer, $\mathbf{B}$ denotes the basis vector inside pth principle layer, and $T_\parallel$ is a two-dimensional translational vector.

Then the Green's function for each $\mathbf{k}_\parallel$ is obtained by

$$\mathrm{g}^a(\epsilon,\mathbf{k}_\parallel)=K^{a,-1}(\epsilon,\mathbf{k}_\parallel), \tag{31}$$

of which all the block elements are calculated by applying the recursive method in Eqs. (25)–(29). Therefore, the on-site matrix elements of the Green's function and normalized Green's function can be evaluated by integrating over the 2D Brillouin zone

$$\mathrm{g}^a_{p\mathbf{B},p\mathbf{B}}(\epsilon)=\frac{1}{\Omega_{\mathrm{BZ}}}\int \mathrm{g}^a_{p\mathbf{B},p\mathbf{B}}(\epsilon,\mathbf{k}_\parallel)d\mathbf{k}_\parallel, \tag{32}$$

$$G_{p\mathbf{B},p\mathbf{B}}(\epsilon)=\frac{1}{\Omega_{\mathrm{BZ}}}\sum_{p'=p-1}^{p+1}\sum_{p'\mathbf{B}'}\int \mathrm{g}^a_{p\mathbf{B},p'\mathbf{B}'}(\epsilon,\mathbf{k}_\parallel)\times \dot{K}^a_{p'\mathbf{B}',p\mathbf{B}}(\epsilon,\mathbf{k}_\parallel)d\mathbf{k}_\parallel, \tag{33}$$

where Ω_{BZ} is the area of the 2D BZ and $\dot{K}^a$ is also tridiagonal matrix.

IV. COHERENT POTENTIAL APPROXIMATION IN EMTO FOR DISORDERED MATERIALS

Coherent potential approximation (CPA) has been a well-established method to do disorder average for systems with substitutional disorders [15,16]. The main idea of CPA is to self-consistently construct an effective medium with translational invariance to give the averaged Green's function of a disordered system, from which the averaged physical quantities can be derived. CPA has already been successfully implemented in the EMTO method by Vitos *et al.* to study the properties of bulk systems, such as alloys [41,42,48,49,52,53]. In this section we apply the CPA to calculate the averaged Green's function of the disordered two-probe electronic device within the EMTO method. Here we only consider the ordered or perfect electrodes, so that the self-energies $\Sigma^a_{l/r}$ in Eqs. (20) and (21) are independent of the disorders in the central device region. As a result, in Eq. (15) for g^a_{cc}, only the atomic function $D^a_R(\epsilon)$ is disordered, depending on the randomly distributed atoms on the lattice sites, while the slope matrix is disorder independent. We thus can introduce an effective atomic function $\mathcal{D}^a_c=\sum_R \mathcal{D}^a_R$ to describe the coherent medium that gives the averaged Green's function $\bar{g}^a_{cc}$, namely

$$\bar{\mathrm{g}}^a_{cc}=\left\{a_c\left[S^a_{cc}-\mathcal{D}^a_c\right]-\Sigma^a_l-\Sigma^a_r\right\}^{-1}. \tag{34}$$

Then, the Green's function g^a of a specific disorder configuration can be given by the following Dyson equation:

$$\mathrm{g}^a=\bar{\mathrm{g}}^a+\bar{\mathrm{g}}^a\Delta\mathrm{g}^a, \tag{35}$$

where the deviation function $\Delta=\sum_R\Delta_R$ and $\Delta_R=a_{Rl}[-D^a_R+\mathcal{D}^a_R]$. By defining T-matrix $T=\Delta(1-\bar{\mathrm{g}}^a\Delta)^{-1}$, the above equation changes to

$$\mathrm{g}^a=\bar{\mathrm{g}}^a+\bar{\mathrm{g}}^a T\bar{\mathrm{g}}^a, \tag{36}$$

where T accounts for the total effect of disorder scatterings. By taking disorder average to the above equation, one finds the CPA condition $\langle T\rangle=0$ to self-consistently solve the effective medium. However, T contains all the complexity of a disordered system, making the problem generally intractable. Further approximation is thus required to solve the CPA equation. To do so, one can rewrite $T=\sum_R T_R$, and $T_R=t_R(1+\bar{g}\sum_{R'}T_{R'})$ where the single-site scattering matrix t_R is defined as $t_R=\Delta_R(1-\bar{\mathrm{g}}^a\Delta_R)^{-1}$ [15,16]. Then the widely used single-site approximation (SSA) can be introduced by neglecting all nonlocal correlation of disorder scattering and local environment effects. The CPA condition $\langle T\rangle=0$ is reduced to a single-site equation

$$\left\langle t^Q_R\right\rangle=\sum_Q c^Q_R t^Q_R=0, \tag{37}$$

where c^Q_R is the concentration of element Q on site R. With above single-site CPA condition, the single-site function $\mathcal{D}^a_R$ for the effective atom on each site can be efficiently solved to obtain the total coherent medium by $\mathcal{D}^a=\sum_R\mathcal{D}^a_R$. However, for stable solution of CPA, instead of solving Eq. (37) directly, we adopted the method of using the coherent interactor [21,34,60,61]. After the CPA self-consistency is achieved, we obtain the averaged and conditionally averaged GFs [62], namely $\bar{\mathrm{g}}$ and $\bar{\mathrm{g}}^Q$, to calculate the related physical quantities including electron density, density of state and transmission coefficient, etc. Furthermore, for the conditionally averaged normalized Green's function, we have in general

$$\begin{aligned}\bar{G}^Q_{R,R}(z)&=\sum_{R'}\bar{\mathrm{g}}^{a,Q}_{R,R'}(z)\dot{K}^{a,Q}_{R',R}\\&=-\bar{\mathrm{g}}^{a,Q}_{R,R}a_R\dot{D}^{a,Q}_R+\sum_{R'}a_{R'}\left(\bar{\mathrm{g}}^a_{R,R'}+\bar{\mathrm{g}}^a_{R,R}t^Q_R\bar{\mathrm{g}}^a_{R,R'}\right)\dot{S}^a_{R',R}.\end{aligned} \tag{38}$$

Here we used the relations

$$\dot{K}^{a,Q}_{R'L',RL}=a_{Rl}\left(\dot{S}^a_{R'L',RL}-\dot{D}^{a,Q}_{R'l'}\delta_{R',R}\delta_{L',L}\right), \tag{39}$$

$$\bar{\mathrm{g}}^{a,Q}_{R,R'}=\left[\bar{\mathrm{g}}^a+\bar{\mathrm{g}}^a t^Q_R\bar{\mathrm{g}}^a\right]_{R,R'}. \tag{40}$$

For a two-probe system with atomic disorder, the conditionally averaged Green's functions can be obtained with the lattice Fourier transformation

$$\begin{aligned}\bar{G}^Q_{p\mathbf{B},p\mathbf{B}}&=-\bar{\mathrm{g}}^{a,Q}_{p\mathbf{B},p\mathbf{B}}a_{p\mathbf{B}}\dot{D}^{a,Q}_{p\mathbf{B}}\\&+\frac{1}{\Omega_{BZ}}\sum_{p'=p-1}^{p+1}\sum_{p'\mathbf{B}'}\int\bar{\mathrm{g}}^a_{p\mathbf{B},p'\mathbf{B}'}(\mathbf{k}_\parallel)a_{p'\mathbf{B}'}\dot{S}^a_{p'\mathbf{B}',p\mathbf{B}}(\mathbf{k}_\parallel)d\mathbf{k}_\parallel\\&+\bar{\mathrm{g}}^a_{p\mathbf{B},p\mathbf{B}}t^Q_{p\mathbf{B}}\sum_{p'\mathbf{B}'}\int\bar{\mathrm{g}}^a_{p\mathbf{B},p'\mathbf{B}'}(\mathbf{k}_\parallel)a_{p'\mathbf{B}'}\dot{S}^a_{p'\mathbf{B}',p\mathbf{B}}(\mathbf{k}_\parallel)d\mathbf{k}_\parallel.\end{aligned} \tag{41}$$

where $\bar{\mathrm{g}}^{a,Q}_{p\mathbf{B},p\mathbf{B}}=\{[-D^{a,Q}_{p\mathbf{B}}-\Omega^a_{p\mathbf{B}}]^{-1}\}$.

V. ELECTRON TRANSPORT: TRANSMISSION COEFFICIENT

To study the quantum transport properties of an electronic device, here we apply the EMTO method to calculate the transmission coefficient which directly gives the conductance and current flow of the device [58,63]. As known, the transmission coefficient for a two-probe device in Fig. 1 can be written in the following form within EMTO:

$$\mathcal{T}(E) = \mathrm{Tr}\left[\mathrm{g}_{cc}^{a,\mathcal{R}}\Gamma_l^a \mathrm{g}_{cc}^{a,\mathcal{A}}\Gamma_r^a\right], \tag{42}$$

in which the quantities $\mathrm{g}_{cc}^{a,\mathcal{R}}$ and $\mathrm{g}_{cc}^{a,\mathcal{A}}$ are the respective retarded and advanced Green's function of the central device region [see Eq. (15)], and the quantities $\Gamma_{l/r}^a$ are the linewidth function characterizing the couplings between the respective left/right electrodes and the central device region [58]. Note that the form of the transmission formula is generally valid for a different basis set, including the orthonormal and nonorthonormal bases [20,24]. Here the linewidth function is given by $\Gamma_{l/r}^a = i(\Sigma_{l/r}^{a,\mathcal{A}} - \Sigma_{l/r}^{a,\mathcal{R}})$ where $\Sigma^{a,\mathcal{R}/\mathcal{A}}$ are the retarded and advanced self-energies [see Eqs. (20)–(23)].

For a specific and ordered device, the calculation of the transmission coefficient is straightforward with Eq. (42) in combination with lattice Fourier transformation. However, for realistic devices, understanding the influences of the inevitable disordered defects or dopants is critical for the development of science and technology. The simulation of a disordered nanoelectronic device requires the computation of the configurationally averaged transmission coefficient. To do so, we need to calculate the disorder average of the transmission operator, namely $\langle \mathrm{g}^{a,\mathcal{R}}\Gamma_l^a \mathrm{g}^{a,\mathcal{A}}\Gamma_r^a\rangle$, which involves the average of two-Green's-function correlators. Here, to simplify the formulation, we only consider the ordered or perfect electrodes, resulting in the disorder independent linewidth functions. However, the effects of disorders in the electrode materials can be studied by introducing the disorders into the electrode buffer layers that are contained in the central device region.

To proceed for the disordered devices, we can apply the relations $\mathrm{g}^{a,\mathcal{R}/\mathcal{A}} = \bar{\mathrm{g}}^{a,\mathcal{R}/\mathcal{A}} + \bar{\mathrm{g}}^{a,\mathcal{R}/\mathcal{A}}T^{\mathcal{R}/\mathcal{A}}\bar{\mathrm{g}}^{a,\mathcal{R}/\mathcal{A}}$ and $\langle T^{\mathcal{R}/\mathcal{A}}\rangle = 0$ to obtain the averaged two-Green's-function correlator as follows:

$$\left\langle \mathrm{g}^{a,\mathcal{R}}\Gamma_l^a \mathrm{g}^{a,\mathcal{A}}\right\rangle = \bar{\mathrm{g}}^{a,\mathcal{R}}\Gamma_l^a\bar{\mathrm{g}}^{a,\mathcal{A}} + \bar{\mathrm{g}}^{a,\mathcal{R}}\Omega_{\mathrm{NVC}}\bar{\mathrm{g}}^{a,\mathcal{A}}, \tag{43}$$

where the "NVC" stands for nonequilibrium vertex correction [2,63–65] and the vertex correction term is defined as $\Omega_{\mathrm{NVC}} = \sum_{R,R'}\langle T_R^{\mathcal{R}}\bar{\mathrm{g}}^{a,\mathcal{R}}\Gamma_l^a\bar{\mathrm{g}}^{a,\mathcal{A}}T_{R'}^{\mathcal{A}}\rangle$ which contains the effects of multiple scattering of disorders. This kind of correlations are accounted for in the NVC. However, it is impossible to obtain an exact solution of this term. For practical simulation, SSA is usually adopted. Applying the SSA, we have $\langle T_R^{\mathcal{R}}\bar{\mathrm{g}}^{a,\mathcal{R}}\Gamma_l^a\bar{\mathrm{g}}^{a,\mathcal{A}}T_{R'}^{\mathcal{A}}\rangle = 0$ if $R' \neq R$ [66]. Then, Ω_{NVC} can be written as a site-diagonal matrix [2,63–65]

$$\Omega_{\mathrm{NVC}} = \sum_R \Omega_{\mathrm{NVC},R} = \sum_R \left\langle T_R^{\mathcal{R}}\bar{\mathrm{g}}^{a,\mathcal{R}}\Gamma_l^a\bar{\mathrm{g}}^{a,\mathcal{A}}T_R^{\mathcal{A}}\right\rangle. \tag{44}$$

Substituting T_R into Eq. (44), we obtain a self-consistent equation for the single-site quantity Ω_{NVC} [2,63,66],

$$\Omega_{\mathrm{NVC},R} = \left\langle t_R^{\mathcal{R}}\bar{\mathrm{g}}^{a,\mathcal{R}}\Gamma_l^a\bar{\mathrm{g}}^{a,\mathcal{A}}t_R^{\mathcal{A}}\right\rangle + \sum_{R'\neq R}\left\langle t_R^{\mathcal{R}}\bar{\mathrm{g}}^{a,\mathcal{R}}\Omega_{\mathrm{NVC},R'}\bar{\mathrm{g}}^{a,\mathcal{A}}t_R^{\mathcal{A}}\right\rangle. \tag{45}$$

Once obtaining the Ω_{NVC}, the averaged transmission function can be calculated by Eqs. (43) and (42). Since the translational invariance is retained after configurational average, we can apply the lattice Fourier transformation to the transmission coefficient as $\mathcal{T}(E) = \frac{1}{N_\parallel}\sum_{k_\parallel}\mathcal{T}(E,k_\parallel)$ where $\mathcal{T}(E,k_\parallel)$ is the $k_\parallel$-resolved transmission coefficient given by

$$\mathcal{T}(E,k_\parallel) = \mathrm{Tr}[\bar{\mathrm{g}}^{a,\mathcal{R}}(k_\parallel)\Gamma_l^a(k_\parallel)\bar{\mathrm{g}}^{a,\mathcal{A}}(k_\parallel)\Gamma_r^a(k_\parallel)] + \mathrm{Tr}[\bar{\mathrm{g}}^{a,\mathcal{R}}(k_\parallel)\Omega_{\mathrm{NVC}}\bar{\mathrm{g}}^{a,\mathcal{A}}(k_\parallel)\Gamma_r^a(k_\parallel)], \tag{46}$$

where Ω_{NVC} is independent of $k_\parallel$ because it is site diagonal. The first term is contributed by the coherent transport, in which the electron transports through the central device region by conserving the momentum $k_\parallel$. The second term is the vertex correction part, including the contribution of transport through interchannel scatterings of disorders, namely diffusive transport. Besides the calculation of the transmission coefficient, in combination with our recently reported generalized nonequilibrium vertex correction method, the quantum transport shot noise and transmission fluctuation can be calculated with the EMTO to further analyze the statistics of the disordered nanoelectronics [38,63].

VI. ELECTRONIC STRUCTURE SELF-CONSISTENCY

By here, Green's function method within the EMTO has been established. In the following, we start to introduce the quantities required for self-consistency of electronic-structure calculation, including electron density, effective muffin tin potential, density of state, etc.

A. Electron density

The full electron density can be divided into the contributions from each Wigner-Seitz (WS) cell, i.e., $n(\mathbf{r}) = \sum_R n_R(\mathbf{r}_R)$. Inside each WS cell, we expand $n_R(\mathbf{r}_R)$ using a set of spherical harmonics

$$\bar{n}_R^Q(\mathbf{r}_R) = \sum_L \bar{n}_{RL}^Q(r_R)Y_L(\hat{r}_R), \tag{47}$$

where

$$\bar{n}_{RL}^Q(r_R) = \int \bar{n}_R^Q(\mathbf{r}_R)Y_L(\hat{r}_R)d\hat{r}_R. \tag{48}$$

In practice, a L truncation in Eq. (47) is applied, which makes the summation finite. By considering Eq. (2) and the associated kink cancellation condition, the orthogonality of the spherical harmonics and the residue theorem, one can obtain, within each potential spheres,

$$\bar{n}_{RL}^Q(r_R) = -\frac{1}{\pi}\sum_{L'L''}\int_0^{\epsilon_F} C_{LL'L''}\phi_{Rl'}^{a,Q}(\epsilon,r_R) \times \mathrm{Im}\,\bar{\mathrm{g}}_{RL',RL''}^{a,Q}(\epsilon+i0^+)\phi_{Rl''}^{a,Q}(\epsilon,r_R)d\epsilon. \tag{49}$$

An important thing should be noticed here is that the normalization function in $\phi^{a,Q}$ may contain nonphysical poles [42].

The remedy is by introducing the correction terms

$$\bar{\mathrm{g}}^{a,Q}_{RL',RL}(z) \to \bar{\mathrm{g}}^{a,Q}_{RL',RL}(z) + \frac{\delta_{L'L}}{a_{Rl}\dot{D}^{a,Q}_{Rl}(z)}\left(\frac{\dot{D}^{a,Q}_{Rl}(z)}{D^{a,Q}_{Rl}(z)} - \sum_{\epsilon^{D}_{Rl}}\frac{1}{z-\epsilon^{D,Q}_{Rl}}\right), \tag{50}$$

where ϵ^{D}_{Rl} is the energy when $D^{a}_{Rl}=0$. Also, to avoid the rapid oscillation along the real axis due to the real poles, we adopt the residue theorem and perform the energy integral on a half-circle contour in the upper complex plane which cuts the real axis at Fermi level and below the bottom of the valence bands. In addition, the Fermi energy of the two-probe device is set to the bulk value of electrodes since we study electronic structure and transport in the limit of equilibrium in the present implementation.

B. Effective potential

In the present implementation of EMTO for device-material simulation, we adopted the spherical cell approximation (SCA) to calculate the overlapping muffin tin potential in Eq. (1) [39]. As an important consequence of SCA, the effective potential $V^{Q}_{R}(r_R)$ for atom Q at site R in Eq. (1) can be given in terms of the spherically averaged charge density, e.g., $\bar{n}^{Q}_{R0}(r_R)$. In our two-probe device calculations, V_{mtz} is fixed to the average value of V_{mtz} in left and right electrodes (we find the electronic structure of central region is actually very insensitive to the used value of V_{mtz}, i.e., Fe/MgO/Fe MTJs). In SCA, the effective spherical potential $V^{Q}_{R}(r_R)$ consists of the contributions from the intracell and intercell interactions [67], namely

$$V^{Q}_{R}(r_R) = V^{Q,I}_{R}(r_R) + V^{\mathrm{SCA},M}(\mathbf{R}). \tag{51}$$

The intracell potential reads

$$V^{Q,I}_{R}(r_R) = -\frac{2Z^{Q}_{R}}{r} + 8\pi\frac{1}{r_R}\int_0^{r_R} r'^{2}_{R}\bar{n}^{Q}_{R0}(r'_R)dr'_R + 8\pi\int_{r_R}^{s_R} r'_R\bar{n}^{Q}_{R0}(r'_R)dr'_R + v^{Q}_{\mathrm{xc},R}(r_R), \tag{52}$$

which contains the nuclei potential in the first term, Hartree potential from electrons inside the potential sphere in the second and third terms, and the exchange-correlation potential $v^{Q}_{\mathrm{xc},R}(r_R)$ in the fourth term. The intercell contribution $V^{\mathrm{SCA},M}_{R}$ accounts for the electrostatic interaction of charges from outside of the potential sphere, usually called Madelung potential. For a bulk system on a lattice with a three-dimensional (3D) periodic boundary condition, the intercell electrostatic field is known as [21]

$$V^{\mathrm{SCA},M}_{\mathrm{bulk}}(\mathbf{r}) = \sum_{\mathbf{B},\mathbf{L}}\chi^{3}_{L}(\mathbf{r}-\mathbf{B})q^{\mathrm{SCA}}_{\mathbf{BL}}, \tag{53}$$

in which χ^{3}_{L} produced by the Lth multipole moments on a 3D lattice can be calculated with the 3D Ewald technique [68], and $q^{\mathrm{SCA}}_{\mathbf{BL}}$ is the Lth multipole moment on the site $\mathbf{B}$ in the unit cell and is calculated within SCA (for disordered system, the disorder averaged value should be used, i.e., $q^{\mathrm{SCA}}_{\mathbf{BL}} = \sum_{Q} c^{Q}_{B} q^{\mathrm{SCA},Q}_{\mathbf{BL}}$) [39,42].

Different from the bulk system, the two-probe device considered in Fig. 1 features the nonperiodicity in the transport z direction, and periodicity in the x-y plane for each principle layer ranging from $ip=-\infty$ to $+\infty$. However, due to the long-range behavior of electrostatic interaction, the contribution of the two semi-infinite electrodes to the central device region is difficult to calculate by direct summation. To provide a general solution to the electrostatics of the infinite two-probe device, we transform the device to an equivalent electrostatic system with finite size and well defined boundary conditions in the transport z direction, while maintaining the periodic boundary condition in the x-y plane. The finite system includes the principle layers ranging from $ip=1$ to np. The two boundaries are defined at the surface planes of the two semi-infinite electrodes (denoted as $z=z_1$ in the layer $ip=0$ and $z=z_2$ in the layer $ip=np+1$) and boundary conditions of the potential are set to the bulk results, i.e., $V^{\mathrm{SCA},M}_{\mathrm{bulk}}$ in Eq. (53), of the respective left and right electrodes. For such a multilayer structure, the electrostatic field can be expressed in the form, as derived in the Appendix,

$$V^{\mathrm{SCA},M}_{\mathrm{two\ probe}}(\mathbf{r}) = \sum_{p=1}^{np}\sum_{\mathbf{pB},\mathbf{L}}\chi^{2}_{L}(\mathbf{r}-p\mathbf{B})q^{\mathrm{SCA}}_{p\mathbf{BL}} + \mathcal{V}_b(\boldsymbol{r}), \tag{54}$$

in which χ^{2}_{L} is the potential produced by the unit Lth multipole moment on a 2D lattice, and can be calculated with the 2D Ewald technique [69–71]. In Eq. (54) the first term is contributed by the multipole moments inside the central device region, and the second term $\mathcal{V}_b(\boldsymbol{r})$ is a required correction to satisfy the boundary conditions at the plane $z=z_1$ and z_2. The potential $\mathcal{V}_b(\boldsymbol{r})$ fulfills the Poisson equation of a finite vacuum system with the boundary conditions. With Eq. (54) the two-probe devices with electrodes of complex materials can be simulated from first principles. In our present implementation, we only consider contribution of the multipole moments $l\leqslant 1$, namely monopole and dipoles, in our calculation of bulk materials and two-probe devices.

C. Density of states

The density of states (DOS) is given by the imaginary part of the conditionally averaged normalized Green's function, i.e.,

$$\bar{\mathrm{D}}^{Q}(\epsilon) = -\frac{1}{\pi}\sum_{RL}\mathrm{Im}\,\bar{G}^{Q}_{RL}(\epsilon). \tag{55}$$

Similarly, the nonphysical poles should be removed by the following correction [42]:

$$\bar{G}^{Q}_{RL}(\epsilon+i0^{+}) \to \bar{G}^{Q}_{RL}(\epsilon+i0^{+}) - \frac{\dot{D}^{a,Q}_{Rl}(\epsilon)}{D^{a,Q}_{Rl}(\epsilon)} + \sum_{\epsilon^{D}_{Rl}}\frac{1}{\epsilon-\epsilon^{D,Q}_{Rl}}. \tag{56}$$

VII. NUMERICAL RESULTS

We have implemented the EMTO based KSDFT into a first-principles nanoelectronic device simulation package, including a bulk-material solver and two-probe device simulator. In this section we present the numerical results to test the

accuracy of our implementation for calculating both the two-probe devices and bulk materials. We calculate the electronic structure of monolayer MoS_2 and black phosphorus with the bulk solver, and calculate the electronic structure and spin-dependent transport property of the Fe/MgO/Fe magnetic tunneling junctions (MTJs) with the device simulator. The DOS results for different systems calculated are compared with the PAW results by using VASP [12]. For the MTJs we study spin-dependent tunneling in both the perfect and disordered devices, and demonstrate the important effects of interfacial disorders on the device functionality. In bulk and two-probe electronic-structure calculations, to ensure the convergence, we use 20 energy points for complex energy contour with the Gaussian quadrature method, and 32×32 uniform k meshes for two-dimensional BZ. (note that monolayer MoS_2 and black phosphorus are 2D systems). A local spin density approximation (LSDA) exchange-correlation functional [72] is employed in our calculations. For the calculation of transmission coefficient, a 200×200 k mesh is adopted to obtain converged spin-dependent conductance. To reach the self-consistency, the Anderson mixing approach is utilized for mixing the muffin tin potential in each iteration [73,74].

A. Bulk: 2D monolayer MoS_2 and black phosphorus

Before investigating the two-probe system, we study the electronic structures of 2D materials to demonstrate the accuracy of the EMTO based bulk solver for systems with low symmetry. Here we calculate the density of states (DOS) for monolayer MoS_2 and black phosphorus which are representative 2D materials (see the Supplemental Material for computation details [75]). In Fig. 2 the results of the EMTO method and PAW method (with VASP) are presented for comparison. For monolayer MoS_2 shown in Fig. 2(a), It is clear that, within a wide range of energy, the DOS of the EMTO method matches very well with the PAW result, i.e., all major DOS peaks of the PAW result are reproduced well by the EMTO method. It is also found that the band gap of MoS_2 with EMTO and PAW methods are very close, although it is significantly underestimated with LDA. Compared to MoS_2 geometrical structure, black phosphorus' structure is more irregular, presenting an important challenge for the muffin tin potential approximation and spherical cell approximation. However, the EMTO results for monolayer black phosphorus, as shown in Fig. 2(b), present overall good agreement with the PAW result, especially for the energies in the range from -4.0 to 2.0 eV. Compared to the good matching of PAW and EMTO results in the whole energy range calculated for monolayer MoS_2, the EMTO and PAW results for the monolayer black phosphorus present a noticeable but small shift in the low energy, while maintaining the same features. It should be mentioned that the EMTO method, with the advantages of overlapping potential sphere and equal-footing treatments of atomic and interstitial regions, features higher accuracy and thus more applicability than the TB-LMTO method. By considering the differences between different methods, the slight deviations between EMTO and PAW results in DOS are acceptable for both the monolayer MoS_2 and black phosphorus. Therefore, we can see the EMTO method can provide an important approach with good accuracy for studying the electronic structure of materials with surfaces/interfaces and low symmetry, providing an important basis for implementing EMTO for simulating electronic devices, in which the interfaces are important.

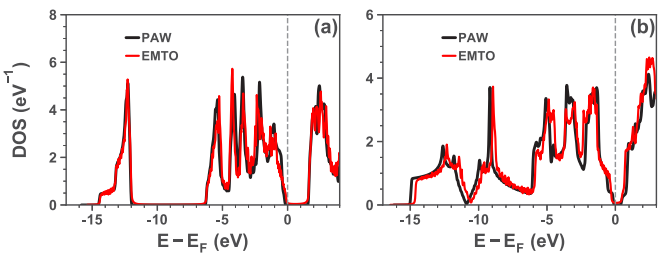

FIG. 2. Total DOS of (a) monolayer MoS_2 and (b) monolayer black phosphorus. Black and red lines represent results of PAW and EMTO methods, respectively.

B. Two-probe device: Fe/MgO/Fe magnetic tunneling junction

For the electronic device simulation, we study the Fe/MgO/Fe MTJs with insulating MgO layers sandwiched by two semi-infinite Fe ferromagnetic electrodes. MgO based MTJ, as a spintronic device, possesses important applications in magnetic sensor [76,77], magnetic random access memory [78,79], etc. MTJ with MgO barrier features strong spin-filtering effect, giving rise to the giant tunnel magnetoresistance (TMR) ratio (even above 1000%) defined as $(R_{AP} - R_P)/R_P$, in which R_{AP} and R_P refer to the junction resistances for the respective antiparallel (APC) and parallel (PC) alignment of the magnetic moments in the two ferromagnetic electrodes [80]. We self-consistently calculate the central device region containing 7 atomic monolayers of MgO and 11 monolayers of Fe as buffer layer on both sides. The electrode Fe is self-consistently calculated with the EMTO based bulk solver (for the computational details, see the Supplemental Material [75]). Because of the closed packed bcc lattice of Fe bulk with high symmetry, the EMTO method can provide very accurate description of the ferromagnetic electrode material Fe. In Fig. 3 we present the EMTO results for the DOS of central device region in PC, and compare with the PAW results [which is obtained by calculating a periodic structure with a unit cell (8 MLs)Fe/(7 MLs)MgO/(9 MLs)Fe].

Figure 3(a) presents the total DOS for the system including 7 MLs MgO and 17 MLs Fe. It is easy to find that the result of the two-probe EMTO method is in very good agreement with the PAW result for the energy ranging from -20.0 to 3.0 eV. This important agreement for both spin channels illustrates the high accuracy of the EMTO method for describing different materials and their interfaces in an electronic device. It is clear that, compared to PAW calculation, the EMTO method provides almost the same energy level alignment between Fe and MgO in the MTJ, which is important for the calculating the electron transport from one electrode Fe to the other through the barrier MgO. Furthermore, because of the important effects of interfaces on the device functionality, we investigate the DOS for the interfacial Fe and MgO atoms in Figs. 3(b) and 3(c), respectively. It is evident that the two-probe EMTO DOSs for both interfacial Fe and MgO atoms match very well with the PAW results (the small deviation

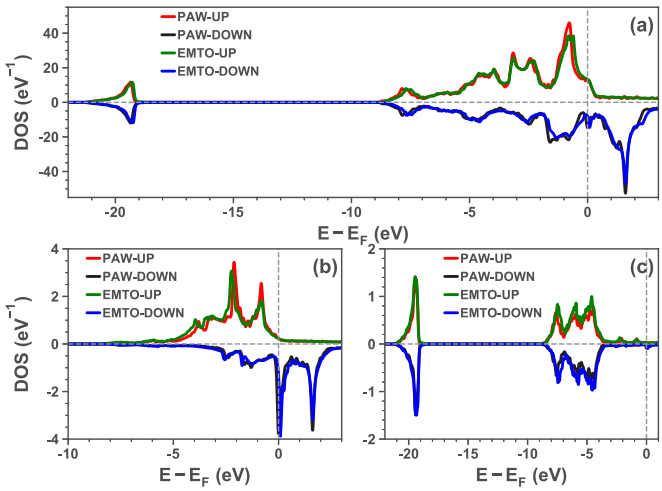

FIG. 3. (a) Total DOS of Fe/MgO/Fe two-probe system and partial DOS of interfacial (b) Fe and (c) MgO atoms. Spin up/down components are indicated by red/black and green/blue colors for results of PAW and EMTO methods, respectively. Here the total DOS is calculated for the central (8 MLs)Fe/(7 MLs)MgO/(9 MLs)Fe.

is negligible), providing an important capability for device-material simulation. For example, for minority spin channel of interfacial Fe atom, as shown in Fig. 3(b), the resonant peak at the Fermi level by PAW, arising from the interfacial state, can be very well reproduced by the EMTO method. Therefore, we can see the EMTO method can provide an accurate description of the electronic structure of the interface between two distinct materials Fe/MgO. In spite of the good accuracy in the electronic structure of device materials, it should be mentioned, due to the use of spherical potential and charge density and SCA in the present implementation of EMTO method, the total energy is not accurate enough for structural relaxation of the electronic device.

C. Spin dependent tunneling in ordered and disordered Fe/MgO/Fe MTJs

Based on the electronic structure with good accuracy, we further study transport properties of perfect and disordered Fe/MgO/Fe MTJs, demonstrating the important capability of the two-probe EMTO device simulator. As shown in Fig. 4, we calculate the $k_\parallel$ resolved transmission coefficient $\mathcal{T}(k_\parallel)$ in

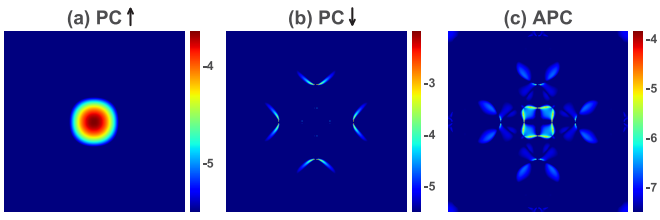

FIG. 4. $k_\parallel$ resolved transmission coefficient $\mathcal{T}(k_\parallel)$ in two-dimensional BZ for (a) spin-up, (b) spin-down channels of clean Fe/MgO/Fe junction in PC, and (c) spin-up (or spin-down) channel of the junction in APC. Here $k_\parallel \in [-\frac{\pi}{a}, \frac{\pi}{a}] \times [-\frac{\pi}{a}, \frac{\pi}{a}]$, where a is the lattice constant in the plane perpendicular to the transport direction. All results are in the base 10 logarithmic scale.

2D BZ at Fermi level for the two spin channels of perfect MTJ in both PC and APC. For spin up channel in PC, shown in Fig. 4(a), the transmission coefficient displays large values around Γ point, i.e., the total conductance is mostly contributed by transmission with small transverse momentum. The reason for such transmission pattern is that a large number of spin-up states from electrodes at Γ point can effectively couple to the Δ_1 band of MgO with the slowest decaying rate [4,80]. For the spin-down channel of PC in Fig. 4(b), the transmission around Γ point is greatly suppressed due to the fact that there is almost no spin-down states around Γ point and states with large transverse momentum cannot couple to the Δ_1 band in MgO due to the coherent transport in the perfect device. However, small areas with high transmission coefficient (hot spots) emerge away from Γ point which arise from the interface resonance, and dominate the transmission of spin-down channel in PC [4,80]. The significant difference between the patterns and magnitude of spin-up and spin-down channels reflects the important spin-dependent tunneling through MTJ. For APC, the spin-up and spin-down channels share the same pattern of transmission coefficient due to the left-right symmetry of the system, as shown in Fig. 4(c). However, since there is no spin flip in the tunneling process and a large mismatch of states in majority and minority spin channels of the respective left and right electrodes, the total transmission of APC are 1–2 order smaller than that of the PC case, e.g., $\mathcal{T}_{\rm APC} = 1.5 \times 10^{-7}$ compared to $\mathcal{T}_{\rm PC} = 6.0 \times 10^{-6}$. As an important result, the MTJ present a giant TMR value as large as 3900%, illustrating the important spin-filtering effect of the junction. Our EMTO calculated results are consistent with previous theoretical studies of perfect Fe/MgO/Fe MTJ.

Beyond calculating the perfect system, as an important advantage, the Green's function based EMTO method can combine with CPA to realize first-principles analysis of disorder effects on the electron transport in the realistic electronic devices. Here we consider disordered oxygen vacancies at left and right Fe/MgO interfaces with the same concentration of 2%. Note that the device still has left-right symmetry after disorder averaging. In the presence of disorder, the transmission can be divided into two parts: Coherent part and vertex part. Coherent transport conserves the transverse momentum same as the perfect device, while the vertex part accounts for the diffusive transport through interchannel scattering. $k_\parallel$ resolved coherent and vertex parts of the transmission coefficients are calculated for spin-up and spin-down channels for the MTJ in PC and APC, as presented in Fig. 5. As shown in Figs. 5(a)–5(d), the coherent parts for different spin channels present patterns similar to results of perfect MTJ in Fig. 4, while the interfacial disorder significantly decreases the amplitudes of coherent transport as expected. The transmission due to interchannel scattering (vertex part) is shown in Figs. 5(e)–5(h) for the disordered MTJ. It is clear the vertex parts present very diffusive patterns in all spin channels. For example, for the spin-up channel in PC, compared to the low transmission for $k_\parallel$ away from Γ point, interfacial disorder scattering can greatly enhance the transmission amplitude by orders. By summing up the vertex and coherent parts, we find the disordered interfacial oxygen vacancies can significantly increase the total transmission of electron for all spin channels in APC, e.g., $\bar{\mathcal{T}}_{\uparrow(\downarrow),\rm APC} = 2.60 \times 10^{-6}$, compared to the

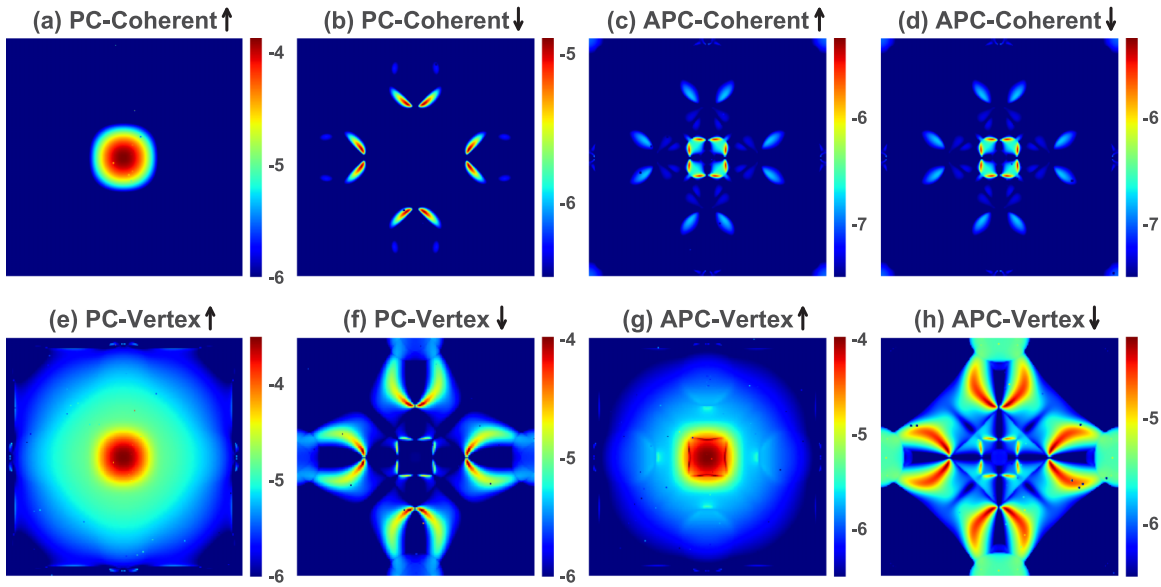

FIG. 5. $k_\parallel$ resolved transmission coefficient $\mathcal{T}(k_\parallel)$ in two-dimensional BZ for coherent and vertex parts of the spin-up and spin-down channels in PC and APC, for Fe/MgO/Fe junction with 2% interfacial oxygen vacancies: (a)–(d) Coherent part and (e)–(h) vertex part. (a) and (e) Spin-up and (b) and (f) spin-down channels in PC. (c) and (g) Spin-up and (d) and (h) spin-down channels in APC. All results are in the base 10 logarithmic scale.

value of perfect MTJ $\bar{\mathcal{T}}_{\uparrow(\downarrow),\mathrm{APC}} = 7.49 \times 10^{-8}$. This important enhancement in the transmission can be attributed to the fact that interfacial disorder induced interchannel scattering can effectively couple the electrode states of both spin channels, other than the Γ state, to the slowly decaying Δ_1 band in MgO, to allow electrons to effectively tunnel though the MTJ [4,80]. As an important consequence, in comparison with the value 3900% of perfect MTJ, the TMR for the calculated disordered MTJ is substantially reduced to 160%, presenting important effects of interfacial oxygen vacancies on the device merit of MTJ. The reduction of TMR due to interfacial oxygen vacancies is in line with previous theoretical and experimental results [4,81,82]. In addition, it is also worth mentioning that, due to the symmetry, vertex parts, featuring very different patterns, present the same total transmission for spin-up and spin-down channels in APC, presenting an important test on our implementation of the EMTO based quantum transport simulation. The implementation of the two-probe EMTO method provides an effective tool for calculating the electronic-structure and electron-transport properties of device materials.

VIII. CONCLUSIONS

In summary, we have implemented the EMTO based first-principles method for simulating the electronic-structure and electron-transport properties of electronic devices. For the device simulation, we consider a material structure with the central device region contacting with different semi-infinite electrodes. Green's function formalism is used to transform the effects of semi-infinite electrodes into self-energies, making the infinite system into a solvable finite device. To efficiently calculate the Green's function of the finite device region, we apply the recursive technique for multilayer structures. Moreover, to realize the simulation of devices with atomic disorders, the coherent potential approximation is combined in the implementation to handle the disorder average. To obtain the disorder averaged transport properties, the vertex correction is implemented to account for the effects of multiple disorder scattering on the electron transport. In the present implementation, the electrostatics is treated within the spherical cell approximation, and the Madelung potential is calculated for the finite central device by enforcing boundary conditions of the electrode potential. To test our implementation, we investigate the monolayer 2D-material MoS_2 and black phosphorus, and the spin-dependent tunneling in the Fe/MgO/Fe magnetic tunneling junction. We find the EMTO electronic structures of the calculated systems agree well with the calculations of the projected augmented wave method. The EMTO transport simulation produces the important spin-filtering effect of the Fe/MgO/Fe junction and the important influence of the interfacial disorders on the spin-dependent tunneling, agreeing well with previous theoretical and experimental studies. With the present EMTO based simulation package, the effects of different materials, interfaces, and disordered defects/impurities on the electron-transport properties can be studied for electronic devices from first principles. Future developments include the extensions to nonequilibrium condition to realize the simulation of operating devices, the combination with full charge density for higher accuracy, etc.

ACKNOWLEDGMENTS

Y.K. acknowledges financial support from ShanghaiTech startup, Innovation Program of Shanghai Municipal Education Commission with Grant No. 15ZZ114, and NSFC with Grant No. 11874265. The authors thank HPC platform of ShanghaiTech University for providing computational facility.

Q.Z. and J.Y. contributed equally to this work.

APPENDIX: SOLVING THE ELECTROSTATIC POTENTIAL FOR A TWO-PROBE DEVICE SYSTEM

For the electrostatic problem of an infinite two-probe system which is nonperiodic in transport z direction, we can transform it to a system which is finite in z direction with known boundary condition for the electrostatics. The finite system has a periodic boundary condition in the x-y plane, and the boundary values take the bulk electrostatic potential in the bulk materials of the left and right electrodes at the respective boundaries $z = z_1$ and z_2, namely

$$\begin{aligned} V_{\text{twop}}^{\text{SCA},M}(\boldsymbol{r})\Big|_{z=z_1} &= V_{\text{bulk,left}}^{\text{SCA},M}(x, y, z_1), \\ V_{\text{twop}}^{\text{SCA},M}(\boldsymbol{r})\Big|_{z=z_2} &= V_{\text{bulk,right}}^{\text{SCA},M}(x, y, z_2). \end{aligned} \tag{A1}$$

For such a finite system with known boundary conditions, the electrostatic potential is composed of two parts: one is caused by charge distribution inside the system, and the other is caused by the boundary condition of the potential in electrodes. For the potential caused by charges, we have

$$V_1^{\text{SCA},M}(\boldsymbol{r}) = \sum_{IP=1}^{NP} \sum_{p\boldsymbol{B},\boldsymbol{L}} \chi_L^2(\boldsymbol{r} - p\boldsymbol{B}) q_{p\boldsymbol{B}\boldsymbol{L}}^{\text{SCA}}, \tag{A2}$$

which is calculated by the 2D Ewald summation due to the periodicity in x-y planes [83].

We then consider the potential due to boundary conditions,

$$\mathcal{V}_b(\boldsymbol{r}) = V_{\text{twop}}^{\text{SCA},M}(\boldsymbol{r}) - V_1^{\text{SCA},M}(\boldsymbol{r}), \tag{A3}$$

with well-defined boundary values $\mathcal{V}_b(\mathbf{r})|_{z=z_1}$ and $\mathcal{V}_b(\mathbf{r})|_{z=z_2}$. Furthermore, the potential $\mathcal{V}_b(\mathbf{r})$ should satisfy the following Poisson's equation:

$$\nabla^2 \mathcal{V}_b(\boldsymbol{r}) = 0, \tag{A4}$$

with the periodic boundary condition in the x-y plane, the $\mathcal{V}_b$ can be expanded as

$$\mathcal{V}_b(\boldsymbol{r}) = \sum_G c_G(z) e^{iG_x x + iG_y y}. \tag{A5}$$

To satisfying the above Poisson's equation, we can find the coefficients

$$\begin{aligned} c_{G\neq 0}(z) &= A_G e^{\sqrt{G_x^2+G_y^2}z} + B_G e^{-\sqrt{G_x^2+G_y^2}z}, \\ c_0(z) &= A_0 z + B_0/ \end{aligned} \tag{A6}$$

For $G \neq 0$, by applying the boundary conditions

$$c_G(z_1) = A_G e^{\sqrt{G_x^2+G_y^2}z_1} + B_G e^{-\sqrt{G_x^2+G_y^2}z_1}, \tag{A7}$$

$$c_G(z_2) = A_G e^{\sqrt{G_x^2+G_y^2}z_2} + B_G e^{-\sqrt{G_x^2+G_y^2}z_2}, \tag{A8}$$

we obtain

$$A_G = \frac{c_G(z_1) e^{\sqrt{G_x^2+G_y^2}z_1} - c_G(z_2) e^{\sqrt{G_x^2+G_y^2}z_2}}{e^{2\sqrt{G_x^2+G_y^2}z_1} - e^{2\sqrt{G_x^2+G_y^2}z_2}}, \tag{A9}$$

$$B_G = \frac{e^{\sqrt{G_x^2+G_y^2}(z_1+z_2)}\left(c_G(z_2) e^{\sqrt{G_x^2+G_y^2}z_1} - c_G(z_1) e^{\sqrt{G_x^2+G_y^2}z_2}\right)}{e^{2\sqrt{G_x^2+G_y^2}z_1} - e^{2\sqrt{G_x^2+G_y^2}z_2}}. \tag{A10}$$

In addition, for $G = 0$, with the boundary conditions

$$c_0(z_1) = A_0 z_1 + B_0, \tag{A11}$$

$$c_0(z_2) = A_0 z_2 + B_0, \tag{A12}$$

we then have

$$A_0 = \frac{c_0(z_1) - c_0(z_2)}{z_1 - z_2}, \quad B_0 = \frac{c_0(z_2) z_1 - c_0(z_1) z_2}{z_1 - z_2}. \tag{A13}$$

After obtaining $\mathcal{V}_b$ with the above formulation, we can find the final electrostatic potential for the central device region due to SCA charges, as presented in Eq. (54) for the self-consistent electronic-structure calculations.

[1] H.-S. P. Wong, IBM J. Res. Dev. **46**, 133 (2002).
[2] Y. Ke, K. Xia, and H. Guo, Phys. Rev. Lett. **100**, 166805 (2008).
[3] Y. Ke, F. Zahid, V. Timoshevskii, K. Xia, D. Gall, and H. Guo, Phys. Rev. B **79**, 155406 (2009).
[4] Y. Ke, K. Xia, and H. Guo, Phys. Rev. Lett. **105**, 236801 (2010).
[5] P. Hohenberg and W. Kohn, Phys. Rev. **136**, B864 (1964).
[6] W. Kohn and L. J. Sham, Phys. Rev. **140**, A1133 (1965).
[7] O. K. Andersen, Phys. Rev. B **12**, 3060 (1975).
[8] D. D. Koelling and G. O. Arbman, J. Phys. F: Metal Phys. **5**, 2041 (1975).
[9] P. E. Blöchl, Phys. Rev. B **50**, 17953 (1994).
[10] D. Sánchez-Portal, P. Ordejón, E. Artacho, and J. M. Soler, Int. J. Quantum Chem. **65**, 453 (1997).
[11] T. L. Beck, Rev. Mod. Phys. **72**, 1041 (2000).
[12] https://www.vasp.at.
[13] http://susi.theochem.tuwien.ac.at.
[14] S. B. Zhang and S.-H. Wei, Phys. Rev. Lett. **92**, 086102 (2004).
[15] P. Soven, Phys. Rev. **156**, 809 (1967).
[16] D. W. Taylor, Phys. Rev. **156**, 1017 (1967).
[17] T. A. Maier, M. Jarrell, T. Prushke, and M. Hettler, Rev. Mod. Phys. **77**, 1027 (2005).
[18] G. D. Mahan, *Many-Particle Physics*, 2nd ed. (Plenum, New York, 1993).
[19] J. Taylor, H. Guo, and J. Wang, Phys. Rev. B **63**, 121104(R) (2001).
[20] J. Taylor, H. Guo, and J. Wang, Phys. Rev. B **63**, 245407 (2001).
[21] I. Turek, V. Drchal, J. Kudrnovský, M. Šob, and P. Weinberger, *Electronic Structure of Disordered Alloys, Surfaces and Interfaces* (Springer US, Boston, MA, 1997).
[22] Y. Xue, S. Datta, and M. A. Ratner, J. Chem. Phys. **115**, 4292 (2001).
[23] Y. Xue, S. Datta, and M. A. Ratner, Chem. Phys. **281**, 151 (2002).
[24] M. Brandbyge, J.-L. Mozos, P. Ordejón, J. Taylor, and K. Stokbro, Phys. Rev. B **65**, 165401 (2002).
[25] S.-H. Ke, H. U. Baranger, and W. Yang, Phys. Rev. B **70**, 085410 (2004).

[26] S. V. Faleev, F. Léonard, D. A. Stewart, and M. van Schilfgaarde, Phys. Rev. B **71**, 195422 (2005).

[27] A. R. Rocha, V. M. García-suárez, S. W. Bailey, C. J. Lambert, J. Ferrer, and S. Sanvito, Nat. Mater. **4**, 335 (2005).

[28] W. Lu, V. Meunier, and J. Bernholc, Phys. Rev. Lett. **95**, 206805 (2005).

[29] D. Waldron, P. Haney, B. Larade, A. MacDonald, and H. Guo, Phys. Rev. Lett. **96**, 166804 (2006).

[30] O. K. Andersen and O. Jepsen, Phys. Rev. Lett. **53**, 2571 (1984).

[31] O. K. Andersen, Z. Pawlowska, and O. Jepsen, Phys. Rev. B **34**, 5253 (1986).

[32] H. L. Skriver, *The LMTO Method: Muffin-Tin Orbitals and Electronic Structure* (Springer, Berlin, 1984).

[33] O. K. Andersen, O. Jepsen, and M. Sob, in *Electronic Band Structure and Its Applications*, edited by M. Yussouff (Springer, Berlin, 1987), pp. 1–57.

[34] V. Kumar, O. K. Andersen, and A. Mookerjee, *Lectures on Methods of Electronic Structure Calculations* (World Scientific, Singapore, 1995).

[35] O. K. Andersen, C. Arcangeli, R. W. Tank, T. Saha-Dasgupta, G. Krier, O. Jepsen, and I. Dasgupta, MRS Proc. **491**, 3 (1997).

[36] O. K. Andersen and T. Saha-Dasgupta, Phys. Rev. B **62**, R16219(R) (2000).

[37] O. K. Andersen, T. Saha-Dasgupta, R. W. Tank, C. Arcangeli, O. Jepsen, and G. Krier, in *Electronic Structure and Physical Properies of Solids*, edited by H. Dreyssé (Springer, Berlin, 2000), pp. 3–84.

[38] J. Yan, S. Wang, K. Xia, and Y. Ke, Phys. Rev. B **95**, 125428 (2017).

[39] L. Vitos, H. Skriver, B. Johansson, and J. Kollár, Comput. Mater. Sci. **18**, 24 (2000).

[40] L. Vitos, Phys. Rev. B **64**, 014107 (2001).

[41] L. Vitos, I. A. Abrikosov, and B. Johansson, Coherent potential approximation within the exact muffin-tin orbitals theory, in *Complex Inorganic Solids: Structural, Stability, and Magnetic Properties of Alloys*, edited by P. E. A. Turchi, A. Gonis, K. Rajan, and A. Meike (Springer US, Boston, MA, 2005), pp. 339–352.

[42] L. Vitos, *Computational Quantum Mechanics for Materials Engineers: The EMTO Method and Applications* (Springer, London, 2007).

[43] L. V. Pourovskii, A. V. Ruban, L. Vitos, H. Ebert, B. Johansson, and I. A. Abrikosov, Phys. Rev. B **71**, 094415 (2005).

[44] L. Vitos, I. A. Abrikosov, and B. Johansson, Phys. Rev. Lett. **87**, 156401 (2001).

[45] P. Olsson, I. Abrikosov, L. Vitos, and J. Wallenius, J. Nucl. Mater. **321**, 84 (2003).

[46] A. Taga, L. Vitos, B. Johansson, and G. Grimvall, Phys. Rev. B **71**, 014201 (2005).

[47] P. Olsson, I. A. Abrikosov, and J. Wallenius, Phys. Rev. B **73**, 104416 (2006).

[48] L. Vitos, J.-O. Nilsson, and B. Johansson, Acta Mater. **54**, 3821 (2006).

[49] D. Music, T. Takahashi, L. Vitos, C. Asker, I. A. Abrikosov, and J. M. Schneider, Appl. Phys. Lett. **91**, 191904 (2007).

[50] B. Alling, A. V. Ruban, A. Karimi, O. E. Peil, S. I. Simak, L. Hultman, and I. A. Abrikosov, Phys. Rev. B **75**, 045123 (2007).

[51] I. A. Abrikosov, A. E. Kissavos, F. Liot, B. Alling, S. I. Simak, O. Peil, and A. V. Ruban, Phys. Rev. B **76**, 014434 (2007).

[52] F. Tian, L. K. Varga, N. Chen, L. Delczeg, and L. Vitos, Phys. Rev. B **87**, 075144 (2013).

[53] F. Tian, L. Delczeg, N. Chen, L. K. Varga, J. Shen, and L. Vitos, Phys. Rev. B **88**, 085128 (2013).

[54] In our implementation we solve the scalar relativistic equation for the partial waves, instead of the Schrödinger equation, to partially take into account some relativistic effects without spin-orbital coupling.

[55] M. Methfessel, Phys. Rev. B **38**, 1537 (1988).

[56] W. A. Strauss, *Partial Differential Equations: An Introduction*, 2nd ed. (Wiley, New York, 2007).

[57] V. Drchal, J. Kudrnovský, and I. Turek, Comput. Phys. Commun. **97**, 111 (1996).

[58] S. Datta, *Quantum Transport: Atom to Transistor* (Cambridge University Press, Cambridge, 2005).

[59] E. M. Godfrin, J. Phys.: Condens. Matter **3**, 7843 (1991).

[60] J. A. Blackman, D. M. Esterling, and N. F. Berk, Phys. Rev. B **4**, 2412 (1971).

[61] J. Kudrnovský and V. Drchal, Phys. Rev. B **41**, 7515 (1990).

[62] The conditionally averaged GF $\bar{g}^{Q}$ is associated with the system in which the nth site is occupied by the fixed Q element, and the disorder average is carried out for the rest of the disordered sites.

[63] J. Yan and Y. Ke, Phys. Rev. B **94**, 045424 (2016).

[64] K. Levin, B. Velický, and H. Ehrenreich, Phys. Rev. B **2**, 1771 (1970).

[65] C. Franz, M. Czerner, and C. Heiliger, J. Phys.: Condens. Matter **25**, 425301 (2013).

[66] B. Velický, S. Kirkpatrick, and H. Ehrenreich, Phys. Rev. **175**, 747 (1968).

[67] J. D. Jackson, *Classical Electrodynamics*, 3rd ed. (Wiley, New York, 1999).

[68] J. C. Slater, *Quantum Theory of Molecules and Solids, Volume 3: Insulators, Semiconductors, and Metals* (McGraw-Hill, New York, 1967).

[69] J. M. MacLaren, S. Crampin, D. D. Vvedensky, and J. B. Pendry, Phys. Rev. B **40**, 12164 (1989).

[70] H. L. Skriver and N. M. Rosengaard, Phys. Rev. B **43**, 9538 (1991).

[71] J. Kudrnovský, I. Turek, V. Drchal, P. Weinberger, S. K. Bose, and A. Pasturel, Phys. Rev. B **47**, 16525 (1993).

[72] S. H. Vosko, L. Wilk, and M. Nusair, Can. J. Phys. **58**, 1200 (1980).

[73] D. G. Anderson, J. ACM **12**, 547 (1965).

[74] V. Eyert, J. Comput. Phys. **124**, 271 (1996).

[75] See Supplemental Material at http://link.aps.org/supplemental/10.1103/PhysRevB.100.075134 for the structure parameters for all the systems calculated with the EMTO method.

[76] J. S. Moodera, L. R. Kinder, T. M. Wong, and R. Meservey, Phys. Rev. Lett. **74**, 3273 (1995).

[77] S. A. Wolf, D. D. Awschalom, R. A. Buhrman, J. M. Daughton, S. von Molnár, M. L. Roukes, A. Y. Chtchelkanova, and D. M. Treger, Science **294**, 1488 (2001).

[78] S. S. P. Parkin, C. Kaiser, A. Panchula, P. M. Rice, B. Hughes, M. Samant, and S.-H. Yang, Nat. Mater. **3**, 862 (2004).

[79] S. Yuasa, T. Nagahama, A. Fukushima, Y. Suzuki, and K. Ando, Nat. Mater. **3**, 868 (2004).

[80] W. H. Butler, X.-G. Zhang, T. C. Schulthess, and J. M. MacLaren, Phys. Rev. B **63**, 054416 (2001).

[81] G. X. Miao, Y. J. Park, J. S. Moodera, M. Seibt, G. Eilers, and M. Münzenberg, Phys. Rev. Lett. **100**, 246803 (2008).

[82] C. Franz, M. Czerner, and C. Heiliger, Phys. Rev. B **88**, 094421 (2013).

[83] C. Kittel, *Introduction to Solid State Physics*, 8th ed. (Wiley, New York, 2004).